Theoretical modelling of hydrodynamic characteristics of a combined column-plate structure based on a novel derivation of mean drift force formulation

Cong, Peiwen
State Key Laboratory of Coastal and Offshore Engineering, Dalian University of Technology

Liu, Yingyi
State Key Laboratory of Coastal and Offshore Engineering, Dalian University of Technology

Gou, Ying
Research Institute for Applied Mechanics, Kyushu University

Teng, Bin
State Key Laboratory of Coastal and Offshore Engineering, Dalian University of Technology

出版情報：Proceedings of the Institution of Mechanical Engineers, Part M: Journal of Engineering for the Maritime Environment. 233 (4), pp.1022-1036, 2018-10-29. SAGE Publications
バージョン：

Theoretical modelling of hydrodynamic characteristics of a combined column-plate structure based on a novel derivation of mean drift force formulation

Peiwen Cong[a]*, Yingyi Liu[a, b], Ying Gou[a] and Bin Teng[a]

[a] State Key Laboratory of Coastal and Offshore Engineering, Dalian University of Technology, Dalian 116024, China

[b] Research Institute for Applied Mechanics, Kyushu University, Kasuga, Fukuoka 816-8580, Japan

Abstract

To improve the seakeeping capability, some devices, such as submerged plates, are often installed on floating structures. The attached plate cannot only suppress the motion response, but also provide an additional immersed body surface that receives fluid action, aggravating the wave loads. In this study, a theoretical model is developed within the context of linear potential theory to study the hydrodynamic characteristics of a floating column with a submerged plate attached at the bottom. The eigenfunction expansion matching method is applied to obtain the velocity potential, based on which the linear wave force and wave runup can be found immediately. A novel derivation of the mean drift force formulation is developed via the application of Green's second identity to the velocity potential and its derivative in finite fluid volume surrounding the body. Formulations that involve control surface can then be derived. With the availability of the velocity potential, semi-analytical solution of the mean drift force on the combined column-plate structure is developed based on respectively the derived and the classic far-field formulations. After conducting convergence tests and validating the theoretical model, detailed numerical analysis is performed thereafter based on the theoretical model. The influence of the plate size, such as the radius and height, on the wave force and the associated wave runup are assessed.

Keywords: Mean drift force; Submerged plate; Control surface; Wave runup

1. Introduction

A submerged plate can be frequently employed as an essential component of many offshore structures, such as spar-type platform and floating wind turbines (FWTs) (Downie et al., 2000; Li et al., 2013; Antonutti et al., 2014). Most proposed semi-submersible FWTs are composed of columns and submerged plates installed at the bottom providing support. The attached plates are designed to increase the added mass and provide extra damping, without obviously changing the displacement or the column size. Consequently, the natural frequency of the structure can be moved out of the dominant frequency range of incident waves. Meanwhile, utilization of submerged plates for other purposes including wave control and coastal morphology control are also promising.

The problem of wave interaction with submerged plates has received considerable attention from researchers. Yu and Chwang (1993) solved the wave scattering over a submerged thin plate by means of eigenfunction expansion method. Martin and Farina (1997) used the hypersingular integral equation to formulate the wave diffraction by a thin plate close enough to the free surface. Molin (2001) proposed a theoretical model to derive the added mass and damping coefficients of periodic arrays of plates. Tao and Thiagarajan (2003a, 2003b) investigated the flow characteristics around an oscillating plate by using the finite difference method. Farina (2010) examined the wave radiation from an oscillating plate and derived an asymptotic approximation for cases of small submergences. Jiang et al. (2014a, 2014b) established analytical solutions for the wave diffraction and radiation problem by a submerged vertical cylinder. Koh and Cho (2016) assessed the performance of double thin plates as motion reduction devices for spar-type platforms. Wang and Zhang (2018) studied on the wave radiation problem by double submerged inclined plates by use of the boundary element method.

Attaching a submerged plate to a floating body can increase the added mass and provide additional damping. Meanwhile, it can also extend the wetted surface that receives fluid loads, giving raise to additional excitations. Different from previous studies, the main attention in this study has no longer been paid on the added mass and damping coefficients associated with an attached plate and their effects on the motion behavior. Instead, our aim is to study particularly the influence of the plate size, such as the radius and height, on the wave force exert on the body and the associated wave runup, which are also closely relevant to the structural design.

In this study, a theoretical model is developed within the context of linear potential theory to study the wave interaction with a stationary combined column-plate structure. The velocity potential is obtained by applying the eigenfunction expansion matching method and the linear wave force and wave runup can be found immediately. The mean drift force is due to the quadratic pressure distributed on the body surface. As remarked in Lee (2007), singularities of the quadratic pressure are present near the hull area with sharp variation of geometry, which makes it difficult to obtain accurate computational results. This study intends to constitute a contribution for overcoming this difficultly. The Green's second identity is applied to the velocity potential and its derivative in finite fluid volume surrounding the body. Formulation that involves control surface can then be derived and the integral on the body surface can be transferred to that written on surfaces surrounding the body. Furthermore, the derived formulation is found to be essentially identical with that in Chen (2006), which is developed by using the variants of Stokes's and Gauss's theorem, for cases of stationary and wall-sided bodies. Semi-analytical solutions of the mean drift force on the combined column-plate structure are then developed based on respectively the derived and the classic far-field formulations. After conducting convergence tests and validating the theoretical model, calculations are conducted for various cases. It can be found that the existence of the plate can lead to obvious amplification of the free-surface oscillation near the front and rear edges of the column at specific frequencies. It is also shown that the in the vertical direction the linear wave force and mean drift force can vanish in certain cases, which suggests that the attached plate can be optimized to decrease the vertical force through adjusting the design parameters.

The remaining part of the present paper is organized as follows: The mathematical problem description is introduced in Section 2. The solution of the wave diffraction problem is presented in Section 3. The calculation of the linear wave force and wave runup is introduced in Section 4. The new derivation of the wave drift force formulation and the calculation of the mean drift force on the combined column-plate structure is introduced in detail in Section 5. Convergence test and validation of the theoretical model is given in Section 6. Numerical computation and analysis are carried out thereafter, with respect to a variety of geometrical parameters in Section 7. Conclusions have been drawn in Section 8 based on the previous analysis.

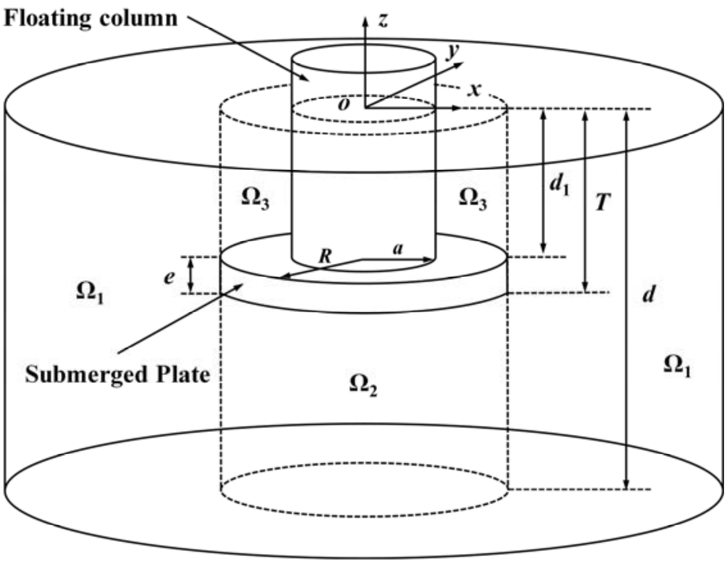

Fig. 1 Definition of the coordinate systems

2. Mathematical Problem

The wave diffraction by a circular column with a submerged plate is considered. The *Oxy* and *Orθ* planes are both located on the undisturbed free surface and the *z*-axis points vertically upward. A circular column with radius a and draft d_1 is floating in the fluid and its axis coincides with the *z*-axis. A submerged plate with radius R and height e, which is coaxial with the column, is attached at the bottom of the column rigidly. The clearance between the plate and seabed is $S = d - T$, where T is the draft of the whole structure and d is the constant water depth.

It is assumed that the fluid is inviscid and incompressible with a constant density ρ, the fluid motion is irrotational, and the wave steepness is small. Thus, the fluid velocity at time t is defined by the gradient of the velocity potential $\Phi(\mathbf{x}, t)$ satisfying Laplace's equation

$$\nabla^2 \Phi(\mathbf{x},\ t) = 0. \tag{1}$$

The velocity potential must satisfy appropriate boundary conditions, namely

$$\frac{\partial^2 \Phi}{\partial t^2} + g\frac{\partial \Phi}{\partial z} = 0, \quad \text{on } z=0; \tag{2}$$

$$\frac{\partial \Phi}{\partial z} = 0, \quad \text{on } z=-d; \tag{3}$$

$$\frac{\partial \Phi}{\partial n} = 0, \quad \text{on } S_b, \tag{4}$$

Further, if the incident wave is time harmonic, the time factor can be separated out and the velocity potential is then expressed as

$$\Phi(\mathbf{x},\ t) = \mathrm{Re}\left[\phi(r,\ \theta,\ z)e^{-i\omega t}\right], \tag{5}$$

where ω represents the wave angular frequency; $i = \sqrt{-1}$.

The presence of the fixed body in the fluid results in diffraction of the incident waves. Then the spatial velocity potential ϕ can be decomposed into the incident potential ϕ_I and the diffraction potential ϕ_D , i.e.,

$$\phi(r,\ \theta,\ z) = \phi_I(r,\ \theta,\ z) + \phi_D(r,\ \theta,\ z). \tag{6}$$

Besides Eqs. (2), (3) and (4), ϕ_D has to satisfy the Sommerfeld radiation condition at a large radial distance from the structure.

Considering linear incident waves propagate to the positive x-direction, ϕ_I is given by:

$$\phi_I(r,\ \theta,\ z) = \sum_{m=0}^{\infty} \varphi_{I,\ m}(r,\ z)\cos m\theta; \tag{7}$$

in which

$$\varphi_{I,\ m}(r,\ z) = -\frac{iAg}{\omega}\frac{\cosh \kappa_0(z+d)}{\cosh \kappa_0 d}\varepsilon_m i^m J_m(\kappa_0 r). \tag{8}$$

In Eq. (8), $\varepsilon_0 = 1$ and $\varepsilon_m = 2$ when $m \geq 1$; $J_m(x)$ are the Bessel functions of order m; A is the amplitude of incident waves; g is the gravitational acceleration; κ_0 is the wave number, satisfying the dispersion relation $\omega^2 = g\kappa_0 \tanh \kappa_0 d$.

3. Solution of Wave Diffraction Problem

The whole fluid domain is divided into three subdomains, i.e., Ω_1, Ω_2 and Ω_3, as shown in Fig. 1. Ω_1 is the exterior domain ($r \geq R$, $-d \leq z \leq 0$), Ω_2 is the domain below the plate ($0 \leq r \leq R$, $-d \leq z \leq -T$), and Ω_3 is the domain above the plate ($a \leq r \leq R$, $-d_1 \leq z \leq 0$). Hereinafter, ϕ_n (n = 1, 2, 3) is used to denote the spatial potential in these subdomains. By means of the eigenfunction expansion method (Yeung, 1981; Calisal and Sabuncu, 1984), ϕ_n can be expanded into Fourier-cosine series in terms of the circumferential coordinate θ

$$\phi_n(r,\ \theta,\ z) = \sum_{m=0}^{\infty} \varphi_{n,\,m}(r,\ z)\cos m\theta, \quad n = 1,\ 2,\ 3, \tag{9}$$

where

$$\varphi_{1,\,m}(r,\ z) = -\frac{iAg}{\omega}\varepsilon_m i^m \left[J_m(\kappa_0 r) Z_0(\kappa_0 z) + \sum_{j=0}^{\infty} A_{m,j} R_{m,j}(\kappa_j r) Z_j(\kappa_j z) \right]; \tag{10a}$$

$$\varphi_{2,\,m}(r,\ z) = -\frac{iAg}{\omega}\varepsilon_m i^m \sum_{l=0}^{\infty} B_{m,\,l} V_{m,\,l}(\lambda_l r) Y_l(\lambda_l z); \tag{10b}$$

$$\varphi_{3,\,m}(r,\ z) = -\frac{iAg}{\omega}\varepsilon_m i^m \sum_{k=0}^{\infty} C_{m,\,k}\left[\beta_{m,\,k} P_{m,\,k}(\mu_k r) + Q_{m,\,k}(\mu_k r)\right] U_k(\mu_k z). \tag{10c}$$

In Eq. (10), $A_{m,j}$, $B_{m,\,l}$ and $C_{m,\,k}$ are unknown coefficients; κ_j ($j \geq 1$) are positive real roots of $-\omega^2 = g\kappa_j \tan(\kappa_j d)$; the eigenvalues λ_l are defined as $\lambda_0 = 1$ and $\lambda_l = l\pi/S$ for $l \geq 1$; μ_0 and wave frequency ω satisfy the dispersion relation $\omega^2 = g\mu_0 \tanh(\mu_0 d_1)$; μ_k ($k \geq 1$) are positive real roots of $-\omega^2 = g\mu_k \tan(\mu_k d_1)$; $R_{m,j}(\kappa_j r)$, $V_{m,\,l}(\lambda_l r)$ and $P_{m,\,k}(\mu_k r)$ are radial functions, defined by

$$R_{m,j}\left(\kappa_j r\right)=\begin{cases}H_m\left(\kappa_0 r\right), & j=0,\\ K_m\left(\kappa_j r\right), & j\ge 1;\end{cases} \tag{11a}$$

$$V_{m,l}\left(\lambda_l r\right)=\begin{cases}\left(\dfrac{r}{R}\right)^m, & l=0,\\ \dfrac{I_m\left(\lambda_l r\right)}{I_m\left(\lambda_l R\right)}, & l\ge 1;\end{cases} \tag{11b}$$

$$P_{m,k}\left(\mu_k r\right)=\begin{cases}J_m\left(\mu_0 r\right), & k=0,\\ I_m\left(\mu_k r\right), & k\ge 1,\end{cases} \tag{11c}$$

in which, $H_m\left(x\right)$ are the first kind of Hankel functions of order m; $I_m\left(x\right)$ and $K_m\left(x\right)$ are the first and second kinds of modified Hankel functions of order m, respectively; $Q_{m,k}\left(\mu_k r\right)$ can be determined according to Eq. (11a) with κ_j and j replaced by μ_k and k respectively; the coefficient $\beta_{m,k}$ is defined as

$$\beta_{m,k}=\begin{cases}-\dfrac{H_m'\left(\mu_0 a\right)}{J_m'\left(\mu_0 a\right)}, & k=0,\\ -\dfrac{K_m'\left(\mu_k a\right)}{I_m'\left(\mu_k a\right)}, & k\ge 1,\end{cases} \tag{12}$$

where the prime appearing in the superscript denotes differentiation with respect to the argument; $Z_j\left(\kappa_j z\right)$, $Y_l\left(\lambda_l z\right)$ and $U_k\left(\mu_k z\right)$ are orthonormal functions given at the intervals $[-d, 0]$, $[-d, -T]$ and $[-d_1, 0]$ respectively, defined by

$$Z_j\left(\kappa_j z\right)=\begin{cases}\dfrac{\cosh\kappa_0\left(z+d\right)}{\cosh\kappa_0 d}, & j=0,\\ \dfrac{\cos\kappa_j\left(z+d\right)}{\cos\kappa_j d}, & j\ge 1;\end{cases} \tag{13a}$$

$$Y_l\left(\lambda_l z\right)=\begin{cases}\dfrac{\sqrt{2}}{2}, & l=0,\\ \cos\lambda_l\left(z+d\right), & l\ge 1;\end{cases} \tag{13b}$$

$$U_k\left(\mu_k z\right)=\begin{cases}\dfrac{\cosh\mu_0\left(z+d_1\right)}{\cosh\mu_0 d_1}, & k=0,\\ \dfrac{\cos\mu_k\left(z+d_1\right)}{\cos\mu_k d_1}, & k\ge 1.\end{cases} \tag{13c}$$

The expressions of the velocity potential are developed to satisfy Laplace's equation, subjecting to all boundary conditions except that at the border of the subdomains, i.e. at $r = R$. The unknown coefficients in these expressions can be determined by imposing the matching condition at $r = R$, based on the assumption that the fluid pressure and the normal velocity are continuous across the border of neighboring subdomains. After truncating the infinite series of the orthogonal functions in Eq. (10) to finite terms, three sets of linear equations can be established containing an equivalent number of unknown coefficients. After solving the linear algebraic system, the unknown coefficients are found and the velocity potentials in each subdomain can be obtained.

4. Calculation of the linear wave force and wave runup

Once the velocity potential is obtained, some other physical quantities of interest may immediately be found. The linear wave runup along the cylinder, ζ, can be determined according to:

$$\zeta = -\frac{1}{g}\frac{\partial \Phi}{\partial t}, \quad \text{on } z = 0. \tag{14}$$

The complex wave runup amplitude, η, is then given by:

$$\eta = A\sum_{m=0}^{\infty}\varepsilon_m i^m \sum_{k=0}^{\infty} C_{m,k}\left[\beta_{m,k}P_{m,k}\left(\mu_k a\right) + Q_{m,k}\left(\mu_k a\right)\right]\cos m\theta. \tag{15}$$

The linear wave force is known by integrating the fluid pressure over the body surface. After integrating in θ and applying the orthogonal relationship, the horizontal force amplitude, f_x, can be expressed as

$$\begin{aligned} f_x = -2iAg\rho\pi \Bigg\{ & R\left[J_1\left(\kappa_0 R\right)\hat{c}_0 + \sum_{j=0}^{\infty} A_{1,j} R_{1,j}\left(\kappa_j R\right)\hat{c}_j \right] \\ & + a\sum_{k=0}^{\infty} C_{1,k}\left[\beta_{1,k}P_{1,k}\left(\mu_k a\right) + Q_{1,k}\left(\mu_k a\right)\right]\hat{d}_k \Bigg\}, \end{aligned} \tag{16}$$

in which

$$\hat{c}_j = \begin{cases} \dfrac{\sinh\kappa_0\left(d-d_1\right) - \sinh\kappa_0 S}{\kappa_0\cosh\kappa_0 d}, & j = 0, \\ \dfrac{\sin\kappa_j\left(d-d_1\right) - \sin\kappa_j S}{\kappa_j\cos\kappa_j d}, & j \ge 1, \end{cases} \tag{17}$$

and

$$\hat{d}_k = \begin{cases} \dfrac{\tanh \mu_0 d_1}{\mu_0}, & k = 0, \\ \dfrac{\tan \mu_k d_1}{\mu_k}, & k \geq 1. \end{cases} \tag{18}$$

Similarly, the vertical force amplitude, f_z, can be written as

$$f_z = 2\pi\rho A g \left[B_{0,\,0} \frac{\sqrt{2}}{4} R^2 + \sum_{l=1}^{\infty} \frac{B_{0,\,l} (-1)^l I_1(\lambda_l R) R}{\lambda_l I_0(\lambda_l R)} - \sum_{k=0}^{N} C_{0,\,k} \Pi_k \right], \tag{19}$$

in which

$$\Pi_k = \begin{cases} \dfrac{\left[\beta_{0,\,0} J_1(\mu_0 R) + H_1(\mu_0 R)\right] R - \left[\beta_{0,\,0} J_1(\mu_0 a) + H_1(\mu_0 a)\right] a}{\mu_0 \cosh \mu_0 d_1}, & k = 0, \\ \dfrac{\left[\beta_{0,\,k} I_1(\mu_k R) - K_1(\mu_k R)\right] R - \left[\beta_{0,\,k} I_1(\mu_k a) - K_1(\mu_k a)\right] a}{\mu_k \cos \mu_k d_1}, & k \geq 1. \end{cases} \tag{20}$$

5. Calculation of the wave drift loads

Three different methods have been developed so far for the computation of the mean drift force. The first one consists of direct pressure integrations on the hull of the body, as described in Pinkster (1980) and Ogilvie (1983), which is called the near-field formulation. The second one was derived in Maruo (1960) and Newman (1967) by applying the momentum theorem, which is called the far-field formulation. The third one was developed by using the variants of Stokes's and Gauss's theorem and takes advantage of a control surface at some distance from the body, as proposed in Chen (2006).

Referring to the established near-field formulation, the wave drift force on a stationary and wall-sided body can be computed by

$$\mathbf{f}^{-} = \overline{-\frac{\rho}{2} \iint_{S_b} \nabla\Phi \cdot \nabla\Phi \mathbf{n} ds + \frac{\rho g}{2} \oint_{\Gamma} \zeta^2 \mathbf{n} dl}, \tag{21}$$

in which all involved quantities in the integrand are of the first order; an over bar indicates the average over a wave period; Γ stands for the intersection of the body surface S_b with the mean free surface (z = 0); $\mathbf{n}$ is the normal vector on S_b and it is positive when pointing out of the fluid domain. For wall-sided bodies, the normal vector along Γ is the same as that on S_b at the same location. The near-field formulation is straightforward and can give all components of the mean drift force. However, for bodies have sharp corners, the quadratic pressure near the corner is singular and it is not easy to obtain accurate computational results through direct pressure integral.

5.1 Calculation based on a novel derivation of wave drift loads formulation

This study intends to constitute a contribution for overcoming above difficulty. After applying Stokes's theorem to a vector function **B**, the following identity can be obtained:

$$\iint_{S_b} \mathbf{n}\cdot\left(\nabla\times\mathbf{B}\right)ds = \oint_{\Gamma} \mathbf{B}\cdot\mathbf{t}dl, \tag{22}$$

in which, the line integral is taken in the counterclockwise sense about Γ; **t** is the unit vector tangent to Γ and oriented in the same direction as the path of integration. If the vector function **B** is supposed to be $\Phi\left(\nabla\Phi\times\mathbf{e}_j\right)$ and the body-surface boundary condition, Eq. (4), is adopted, Eq. (22) can be written as:

$$\iint_{S_b}\left(\nabla\Phi\cdot\nabla\Phi\right)n_j ds = \iint_{S_b}\Phi\frac{\partial}{\partial n}\left(\frac{\partial\Phi}{\partial x_j}\right)ds - \oint_{\Gamma}\Phi\left(\nabla\Phi\times\mathbf{e}_j\right)\cdot\mathbf{t}dl. \tag{23}$$

in which, $\mathbf{e}_j$ ($j = 1, 2, 3$) represents the unit vectors in the x, y or z direction respectively; $x_1 = x$, $x_2 = y$, and $x_3 = z$; $n_1 = n_x$, $n_2 = n_y$, and $n_3 = n_z$.

A finite fluid volume limited by S_b, S_c, and S_f' is considered, in which S_c represents a fictitious (control) surface surrounding the body and S_f' is the mean free surface limited by Γ and the intersection of S_c with z = 0. As the velocity potential and its derivative both satisfy the Laplace's equation, by applying Green's second identify in the control fluid volume and making use of Eqs. (3) and (4), we can have:

$$\iint_{S_b}\Phi\frac{\partial}{\partial n}\left(\frac{\partial\Phi}{\partial x_j}\right)ds = \iint_{S_c+S_f'}\left[\frac{\partial\Phi}{\partial x_j}\frac{\partial\Phi}{\partial n} - \Phi\frac{\partial}{\partial n}\left(\frac{\partial\Phi}{\partial x_j}\right)\right]ds. \tag{24}$$

Then Eq. (23) can be rewritten as:

$$\iint_{S_b}\left(\nabla\Phi\cdot\nabla\Phi\right)n_j ds = \iint_{S_c+S_f'}\left[\frac{\partial\Phi}{\partial x_j}\frac{\partial\Phi}{\partial n} - \Phi\frac{\partial}{\partial n}\left(\frac{\partial\Phi}{\partial x_j}\right)\right]ds - \oint_{\Gamma}\Phi\left(\nabla\Phi\times\mathbf{e}_j\right)\cdot\mathbf{t}dl. \tag{25}$$

The integrals on the right-hand side of Eq. (25) contain second-order derivative of the first-order velocity potential. As it is difficult to achieve high accuracy of the second-order derivative, care must be taken in dealing with these trouble terms. Based on the assumption that the control surface intersects vertically with $z = 0$, the integral over S_c can be expressed as one only containing the first-order derivative plus a line integral by use of Stokes's theorem:

$$\iint_{S_c}\left[\frac{\partial \Phi}{\partial x_j}\frac{\partial \Phi}{\partial n}-\Phi\frac{\partial}{\partial n}\left(\frac{\partial \Phi}{\partial x_j}\right)\right]ds=\iint_{S_c}\left[2\frac{\partial \Phi}{\partial x_j}\frac{\partial \Phi}{\partial n}-\left(\nabla\Phi\cdot\nabla\Phi\right)n_j\right]ds-\oint_{\Gamma_c}\Phi\left(\nabla\Phi\times\mathbf{e}_j\right)\cdot\mathbf{t}dl, \tag{26}$$

in which, Γ_c represents the intersection of S_c with $z = 0$ and the line integral is taken in the clockwise sense about Γ_c.

From Eq. (5), it is noted the velocity potential can be expressed in time-spatial decomposed form. For the case of $j = 1$, the integral over S_f' on the right-hand side of Eq. (25) can then be expressed as follows after imposing Eq. (2)

$$\iint_{S_f'}\left[\frac{\partial \Phi}{\partial x}\frac{\partial \Phi}{\partial z}-\Phi\frac{\partial}{\partial z}\left(\frac{\partial \Phi}{\partial x}\right)\right]ds=\frac{1}{g}\iint_{S_f'}\frac{\partial}{\partial t}\left(-\frac{\partial \Phi}{\partial x}\frac{\partial \Phi}{\partial t}+\Phi\frac{\partial^2 \Phi}{\partial x\partial t}\right)ds. \tag{27}$$

It is obvious that the integral on the right-hand side of Eq. (27) gives zero mean in one period, which indicates

$$\overline{\iint_{S_f'}\left[\frac{\partial \Phi}{\partial x}\frac{\partial \Phi}{\partial z}-\Phi\frac{\partial}{\partial z}\left(\frac{\partial \Phi}{\partial x}\right)\right]ds}=0. \tag{28}$$

Therefore, for the case of $j = 1$, the integral over S_f' gives no contribution to the mean drift force. Meanwhile, for the case of $j = 3$, the integral over S_f' is possible to be expressed as one only containing the first-order derivative plus a line integral by use of Green's theorem. By imposing Eq. (4), the order of the derivatives can be reduced as follows:

$$\iint_{S_f'}\left(\frac{\partial \Phi}{\partial z}\frac{\partial \Phi}{\partial z}-\Phi\frac{\partial^2 \Phi}{\partial z^2}\right)ds=\iint_{S_f'}\left[2\frac{\partial \Phi}{\partial z}\frac{\partial \Phi}{\partial z}-\left(\nabla\Phi\cdot\nabla\Phi\right)n_z\right]ds+\oint_{\Gamma_c}\Phi\frac{\partial \Phi}{\partial n}dl, \tag{29}$$

in which, the line integral is taken in the counterclockwise sense about Γ_c.

Then by introducing Eq. (25) with $j = 1$ into Eq. (21) and making use of Eqs. (26)

and (28), the following formulation for $\overline{f_x^-}$ can be obtained.

$$\overline{f_x^- = -\frac{\rho}{2}\iint_{S_c}\left[2\frac{\partial\Phi}{\partial x}\frac{\partial\Phi}{\partial n}-\left(\nabla\Phi\cdot\nabla\Phi\right)n_x\right]ds-\frac{\rho}{2}\oint_{\Gamma_c}\Phi\frac{\partial\Phi}{\partial z}n_x dl+\frac{\rho}{2}\oint_{\Gamma}\left(g\zeta^2-\Phi\frac{\partial\Phi}{\partial z}\right)n_x dl.} \tag{30}$$

If Eqs. (2) and (14) are adopted, the line integral along Γ in Eq. (30) can be further expressed as:

$$\oint_{\Gamma}\left(g\zeta^2-\Phi\frac{\partial\Phi}{\partial z}\right)n_x dl=\frac{1}{g}\oint_{\Gamma}\frac{\partial}{\partial t}\left(\Phi\frac{\partial\Phi}{\partial t}\right)n_x dl. \tag{31}$$

It is obvious that the integral on the right-hand side in Eq. (31) gives zero mean in one period, which indicates

$$\overline{\oint_{\Gamma}\left(g\zeta^2-\Phi\frac{\partial\Phi}{\partial z}\right)n_x dl}=0. \tag{32}$$

Eq. (32) is also true with Γ replaced by Γ_c. Then by making use of Eq. (32), Eq. (30) can be rewritten as

$$\overline{f_x^- = -\frac{\rho}{2}\iint_{S_c}\left[2\frac{\partial\Phi}{\partial x}\frac{\partial\Phi}{\partial n}-\left(\nabla\Phi\cdot\nabla\Phi\right)n_x\right]ds-\frac{\rho g}{2}\oint_{\Gamma_c}\zeta^2 n_x dl.} \tag{33}$$

By introducing Eq. (25) with $j = 3$ into Eq. (21) and making use of Eqs. (26) and (29), the following formulation for $\overline{f_z^-}$ can be obtained.

$$\overline{f_z^- = -\frac{\rho}{2}\iint_{S_c+S_f'}\left[2\frac{\partial\Phi}{\partial z}\frac{\partial\Phi}{\partial n}-\left(\nabla\Phi\cdot\nabla\Phi\right)n_z\right]ds.} \tag{34}$$

Thus, the mean drift force in the vertical direction is given by the integral on the control surface S_c and the limited free surface S_f'.

Now the formulation for the computation of the wave drift force, Eqs. (33) and (34), is derived based on the application of Green's second identity in a finite fluid volume surrounding the body. It can be noted that the derived formulation is equivalent to that obtained in Chen (2007) by using the variants of Stokes's and Gauss's theorem.

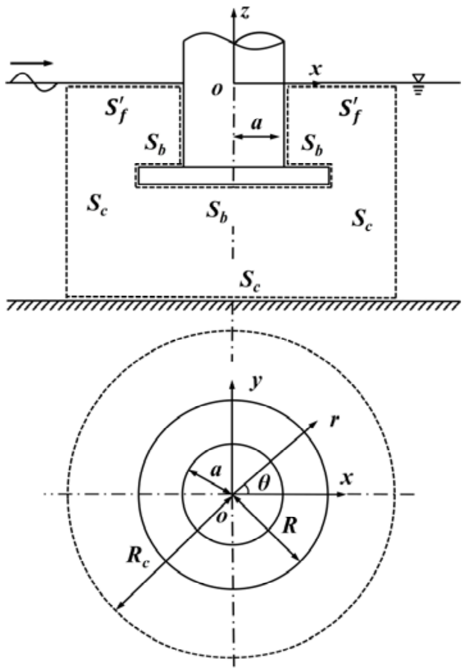

Fig. 2 Definition of control surface in the numerical implementation

With the availability of the velocity potential and based on the derived formulation, the mean drift force on the combined column-plate structure can be evaluated. The form of the control surface S_c can be arbitrary. To facilitate the numerical implementation, hereinafter, the control surface is made to be composed of a cylindrical surface defined by $r = R_c$ and $-d \le z \le 0$, and a limited sea-bed surface defined by $z = -d$ and $0 \le r \le R$. Fig. 2 gives the definition of the control surface in the numerical implantation. For vertically axisymmetric bodies, the surface integrals in Eqs. (33) and (34) can be reduced to line integrals after integrating in θ and applying orthogonality. Thus, by introducing Eqs. (9) and (10), the mean drift force on the combined column-plate structure can be calculated according to:

$$f_x^- = \mathrm{Re}\left\{-\frac{\rho\pi}{4}\sum_{m=0}^{\infty}\left[\int_{-d}^{0}\hat{p}_{1,m}(R_c, z)dz + \hat{q}_{1,m}(R_c, 0)\right]\right\}; \tag{35}$$

$$\begin{aligned} f_z^- = \mathrm{Re}\Bigg\{-\frac{\rho\pi}{4}\sum_{m=0}^{\infty}\Bigg[&\int_{-d}^{0}\hat{u}_{1,m}(R_c, z)dz + \int_{a}^{R}\hat{v}_{3,m}(r, 0)dr + \int_{R}^{R_c}\hat{v}_{1,m}(r, 0)dr \\ &+\int_{0}^{R}\hat{w}_{2,m}(r, -d)dr + \int_{R}^{R_c}\hat{w}_{1,m}(r, -d)dr\Bigg]\Bigg\}, \end{aligned} \tag{36}$$

in which

$$\hat{p}_{n,m}(r,z)=\frac{2}{\varepsilon_m}\left(\frac{\partial\varphi_{n,m}}{\partial r}\frac{\partial\varphi^*_{n,m+1}}{\partial r}+\frac{m+1}{r}\varphi_{n,m+1}\frac{\partial\varphi^*_{n,m}}{\partial r}-\frac{m}{r}\varphi_{n,m}\frac{\partial\varphi^*_{n,m+1}}{\partial r}\right.$$
$$\left.-\frac{m}{r}\frac{m+1}{r}\varphi_{n,m}\varphi^*_{n,m+1}-\frac{\partial\varphi_{n,m}}{\partial z}\frac{\partial\varphi^*_{n,m+1}}{\partial z}\right)r; \tag{37a}$$

$$\hat{q}_{n,m}(r,z)=\frac{2}{\varepsilon_m}\left(\frac{\omega^2}{g}\varphi_{n,m}\varphi^*_{n,m+1}\right)r, \tag{37b}$$

and

$$\hat{u}_{n,m}(r,z)=\frac{2}{\varepsilon_m}\left(2\frac{\partial\varphi_{n,m}}{\partial z}\frac{\partial\varphi^*_{n,m}}{\partial r}\right)r; \tag{38a}$$

$$\hat{v}_{n,m}(r,z)=\frac{2}{\varepsilon_m}\left(\frac{\omega^4}{g^2}\varphi_{n,m}\varphi^*_{n,m}-\frac{\partial\varphi_{n,m}}{\partial r}\frac{\partial\varphi^*_{n,m}}{\partial r}-\frac{m^2}{r^2}\varphi_{n,m}\varphi^*_{n,m}\right)r; \tag{38b}$$

$$\hat{w}_{n,m}(r,z)=\frac{2}{\varepsilon_m}\left(\frac{\partial\varphi_{n,m}}{\partial r}\frac{\partial\varphi^*_{n,m}}{\partial r}+\frac{m^2}{r^2}\varphi_{n,m}\varphi^*_{n,m}\right)r. \tag{38c}$$

In Eqs. (35) and (36), 'Re' indicates that the real part is to be taken. In the numerical implementation, Romberg quadrature method is used to control the accuracy of the line integral in Eqs. (35) and (36).

5.2 Calculation based on the classic far-field formulation

The mean drift force can also be deduced from the quantities at far field. The far-field formulation is restricted to give the components in the horizontal directions and the moment around vertical axis. The expression of f_x^- given in Mei et al. (2005) is reported below:

$$f_x^- = -\overline{\iint_{S_\infty}\left[P\cos\theta+\rho U_r\left(U_r\cos\theta-U_\theta\sin\theta\right)\right]ds}, \tag{39}$$

in which, S_∞ is a cylindrical surface located at infinity; $\boldsymbol{U}$ denotes the fluid velocity and can be expressed in terms of gradient of the velocity potential; P is the pressure term on the control surface and can be determined based on Bernoulli equation. With all these manipulations, the following expression can be obtained (Mei, et al, 2005):

$$f_x^- = -\int_0^{2\pi} \rho r d\theta \cos\theta \left\{ \int_{-d}^{0} dz \frac{1}{2} \left[\overline{\left(\frac{\partial \Phi}{\partial r} \right)^2} - \overline{\left(\frac{\partial \Phi}{\partial z} \right)^2} \right] + \frac{\omega^2}{4g} |\phi|_{z=0}^2 \right\}, \tag{40}$$

in which, r tends to infinity. At far field, the contribution from the evanescent modes to the diffraction potential is neglected. By using the asymptotic expressions for Bessel functions, the diffraction potential for large r can be expressed in an asymptotic form. When the wave interaction with the combined column-plate structure is considered, ϕ_1 at far field is given by:

$$\phi_1 = -\frac{igA}{\omega} \left[e^{i\kappa_0 r \cos\theta} + \sqrt{\frac{2}{\pi \kappa_0 r}} e^{i\left(\kappa_0 r - \frac{\pi}{4}\right)} \sum_{m=-\infty}^{+\infty} \Lambda_m \cos m\theta \right] Z_0(\kappa_0 z), \tag{41}$$

in which,

$$\Lambda_m = \varepsilon_m i^m A_{m,0} e^{-\frac{m\pi}{2} i}. \tag{42}$$

By inserting Eq. (41) into Eq. (40) and applying the stationary phase method to the integrals, Eq. (40) can be rewritten as

$$f_x^- = -\frac{\rho g A^2}{\kappa_0} \frac{2\kappa_0 d + \sinh 2\kappa_0 d}{2 \sinh 2\kappa_0 d} \mathrm{Re} \left[\sum_{m=0}^{+\infty} 2 \left(\frac{1}{\varepsilon_m} \Lambda_m \Lambda_{m+1}^* + \Lambda_m \right) \right]. \tag{43}$$

6. Convergence Test and Validation

In order to ensure that present results are free from the influence of the truncation number, convergence of the theoretical model is examined. Hereinafter, $\rho g a^2 A$ and $\rho g a A^2$ are used to nondimensionalize the linear and mean drift force respectively. As illustrated in Bachynski et al. (2014), the dimensional supporting-column diameter in a wind turbine system can be around 12 m. The examination considers the cases that the draft of the structure keeps unchangeable at $T/a = 1$ and the plate radius keeps 1.5 times the column radius ($R/a = 1.5$). At the meantime, the plate height varies as $e/a = 0$, 0.05, 0.1 and 0.2. The water depth is constant as $d/a = 3$. The accuracy of the calculation for the linear wave force is mainly influenced by the number of eigenmodes N. Fig. 3 shows the linear wave force amplitude with varying N. As to the calculation of the mean drift force, not only the number of eigenmodes N, but also that of Fourier modes M, can affect the accuracy. Figs. 4-6 present the examination on the convergence of the mean drift force with respect to varying M and N. In these figures, the mean drift force results based on the derived and the classic far-field formulations are referred as 'NF' and 'FF' respectively. It can be seen that, regardless of the size of the structure, the convergence is satisfactory. Moreover, it can be concluded that 15 Fourier coefficients and 100 eigenmodes are sufficient to guarantee a satisfactory accuracy. Therefore, $M = 15$ and $N = 100$ are used in all the subsequent computations.

The dependence of the calculation on the control surface is then examined when the derived mean drift force formulation is used. Fig. 7 presents the mean drift force results for different cases of control surface, in which R_c is varied as $R + d$, $R + 2d$ and $R + 5d$. $R_c = R + d$ has been used in the previous convergence test. It can be seen the different cases give almost the same results and $R_c = R + d$ is then used in all the subsequent computations. Furthermore, in order to make sure that the theoretical model is valid and reliable to a convinced degree, a comparison between the mean drift force results based on the derived and the classic far-field formulations is made. From the comparison listed in Table 1, it can be noted excellent agreement is obtained between the results.

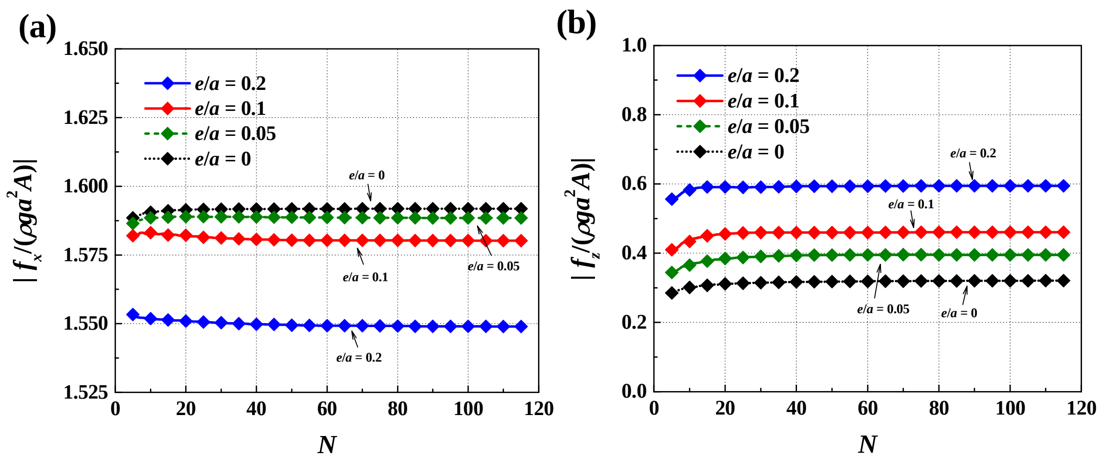

Fig. 3 Convergence test on the linear wave force amplitude with respect to the number of eigenmodes N at $\kappa_0 a = 2.0$ ($T/a = 1$, $R/a = 1.5$, $d/a = 3$) (a) horizontal force (b) vertical force

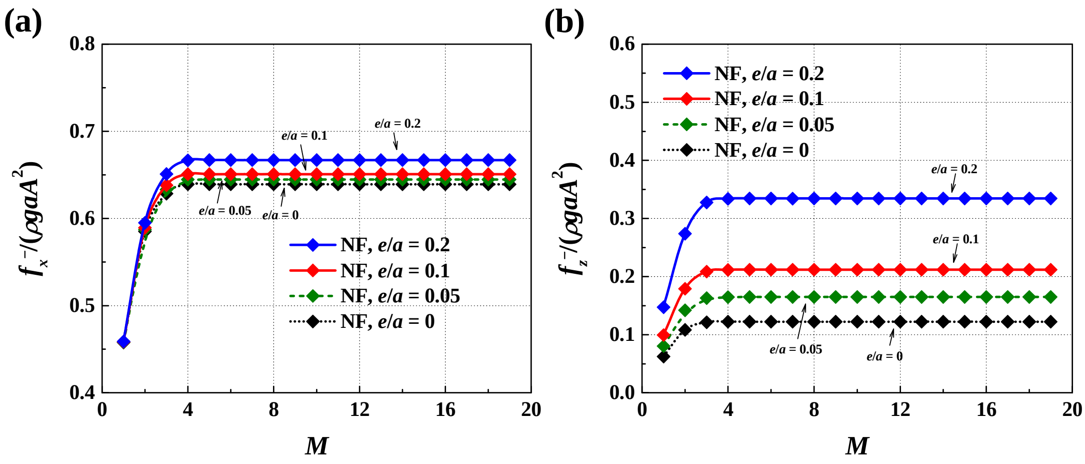

Fig. 4 Convergence test on the mean drift force based on the derived formulation with respect to the number of Fourier modes M at $\kappa_0 a = 2.0$ ($T/a = 1$, $R/a = 1.5$, $d/a = 3$) (a) horizontal force (b) vertical force

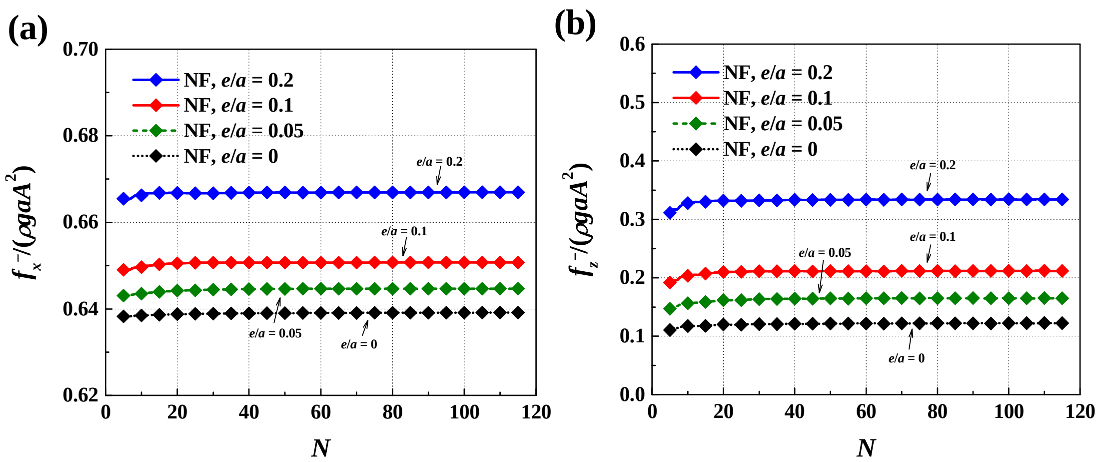

Fig. 5 Convergence test on the mean drift force based on the derived formulation with respect to the number of eigenmodes N at $\kappa_0 a = 2.0$ ($T/a = 1$, $R/a = 1.5$, $d/a = 3$) (a) horizontal force (b) vertical force

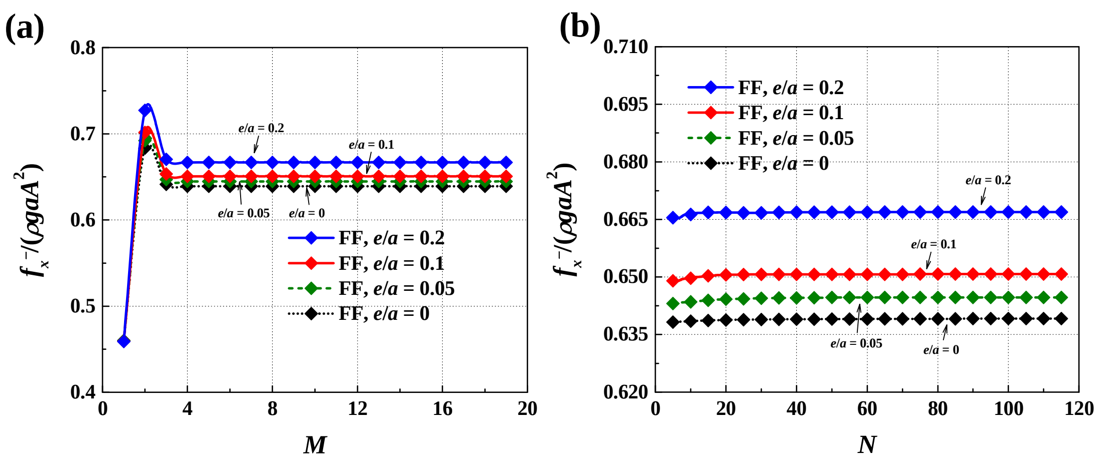

Fig. 6 Convergence test on the mean drift force based on the far-field formulation with respect to the number of Fourier modes M and eigenmodes N at $\kappa_0 a = 2.0$ ($T/a = 1$, $R/a = 1.5$, $d/a = 3$) (a) M (b) N

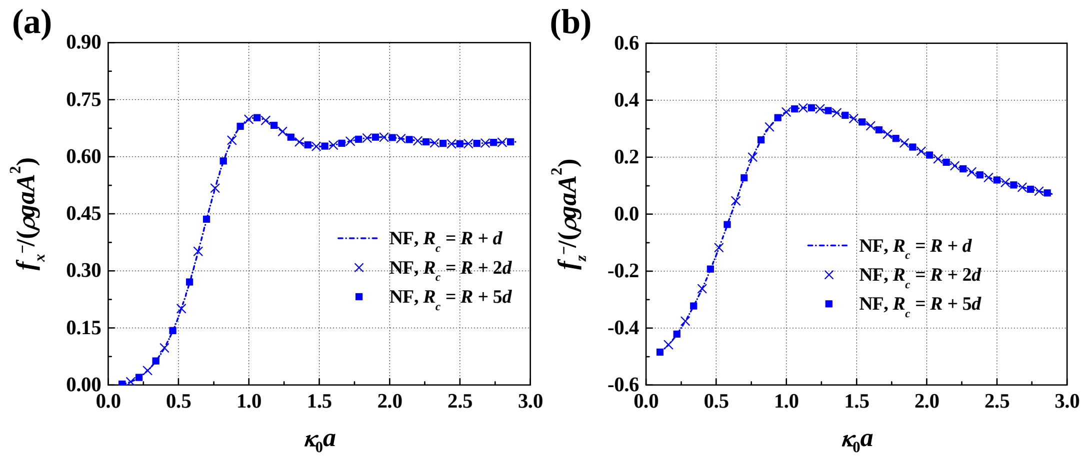

Fig. 7 Comparison of the mean drift force based on different values of R_c at $\kappa_0 a$ = 2.0 (T/a = 1, R/a = 1.5, e/a = 0.1, d/a = 3) (a) horizontal force (b) vertical force

Table 1 Comparison of the normalized mean drift force, $f_x^- / \left(\rho g a A^2\right)$, based on the derived and the far-field formulations at different wave frequencies (T/a = 1, R/a = 1.5, d/a = 3)

e/a =	0		0.05		0.1		0.2	
$\kappa_0 a$ =	NF	FF	NF	FF	NF	FF	NF	FF
1.0	0.664	0.664	0.682	0.682	0.699	0.699	0.738	0.738
1.2	0.654	0.654	0.666	0.666	0.677	0.677	0.704	0.704
1.4	0.617	0.617	0.625	0.625	0.633	0.633	0.653	0.653
1.6	0.615	0.615	0.622	0.622	0.631	0.631	0.653	0.653
1.8	0.632	0.632	0.639	0.639	0.647	0.647	0.668	0.668
2.0	0.639	0.639	0.645	0.645	0.651	0.651	0.667	0.667

7. Numerical Results and Discussion

A comprehensive study is then performed to discuss the effects of the attached plate on the wave force and the associated wave runup. In all the subsequent calculations, the draft of structure keeps constant as T/a = 1 and the water depth is d/a = 3.

7.1 Linear Wave Runup

The effects of the attached plate on the linear wave runup amplitude at three different locations around the body are shown in Fig. 8. The wave runup amplitude is plotted versus the normalized wave number $\kappa_0 a$ in the cases of varying radius R and a constant plate height e/a = 0.1. All curves in Fig. 8 are asymptotically getting close to 1 as $\kappa_0 a$ approaches zero, a state of no wave transformation at all.

A larger plate radius can cause a larger wave runup at the rear edge of the column (r

= a, $\theta = 0$, see Fig. 8(a)). From Fig. 8(a), it is also found that the wave runup amplitude is always less than that of incident waves when $R = a$. However, this is not the case when $R > a$. An obviously amplified wave runup occurs around $\kappa_0 a = 0.67$ when $R > a$, and the amplification gradually weakens as R decreases. After shoaling into shallower region over the plate, waves would undergo complicated transfer process. As pointed by Yu (2002) in studying the wave scattering by a submerged plate that such transfer process could induce obvious amplification of the free-surface oscillation over the plate due to the phase interaction between the flows over and below the plate. Therefore, obviously amplified wave runup can be observed in this study after including the effects of the plate. Beyond the peak point, the wave runup amplitude decays quickly as $\kappa_0 a$ increases until less than that of incident waves. This can be attributed to the sheltering effects provided by the column to the rear zone behind the structure. In Fig. 8(b), each curve is characterized by an obvious peak, which gradually decreases and moves to the high frequency region as R decreases. Beyond that peak point, influence from the plate radius tends to be minor. At the front edge of the column ($r = a$, $\theta = \pi$, see Fig. 8(c)), the wave runup firstly grows quickly until reaches the peak, which is reduced as the radius of the plate approaches that of the column. Beyond the peak point, the wave runup firstly falls quickly and then tends to behave stable in the high frequency region.

Fig. 9 presents the linear wave runup amplitude at three selected locations for different plate height e with the plate radius keeps constant as $R/a = 1.5$. Effects of the plate height are similar to that of the plate radius. Generally, when getting closer to the free surface, the plate can have more significant effects on the wave scattering process by the structure, which is a consequence of the exponential decay of wave motion in the gravity direction.

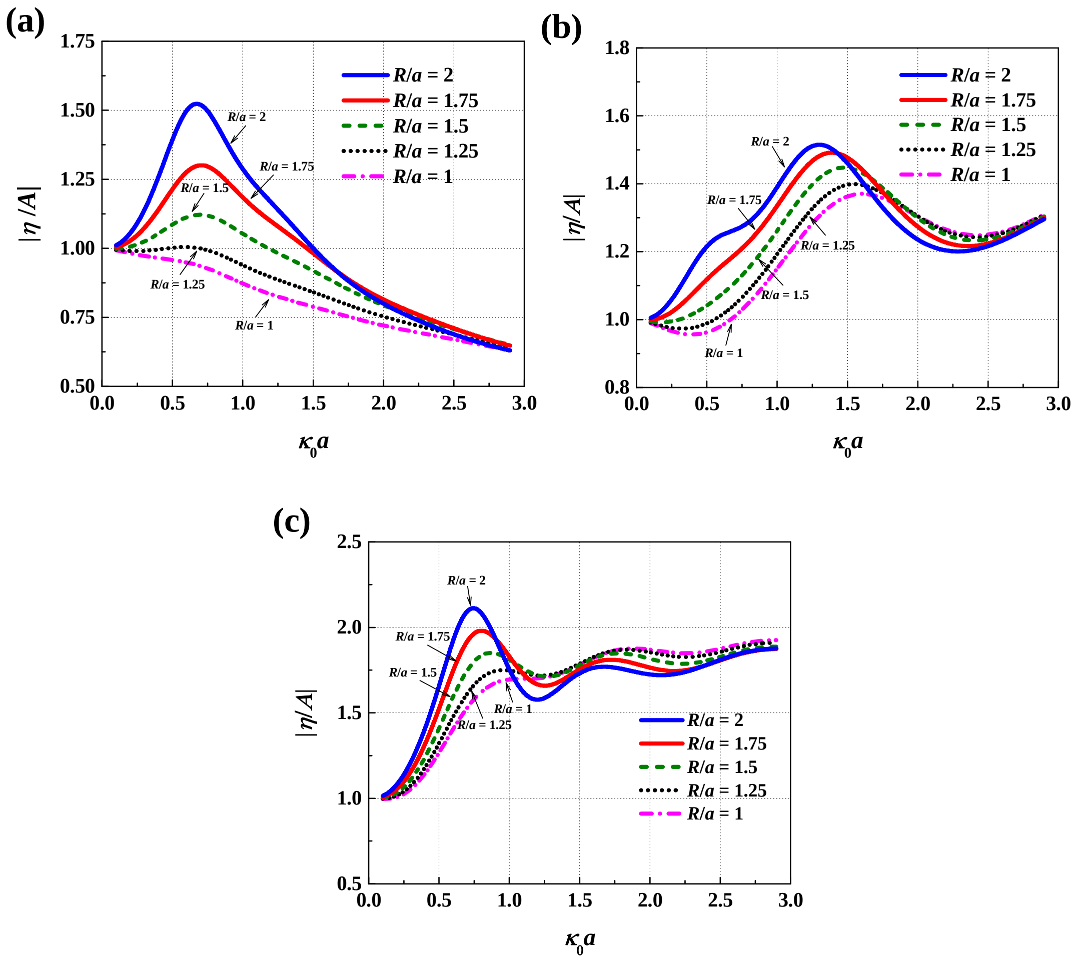

Fig. 8 Normalized linear wave runup amplitude at three locations around the body with different plate radius (T/a = 1, e/a = 0.1, d/a = 3) (a) $r = a$, $\theta = 0$ (b) $r = a$, $\theta = \pi/2$ (c) $r = a$, $\theta = \pi$

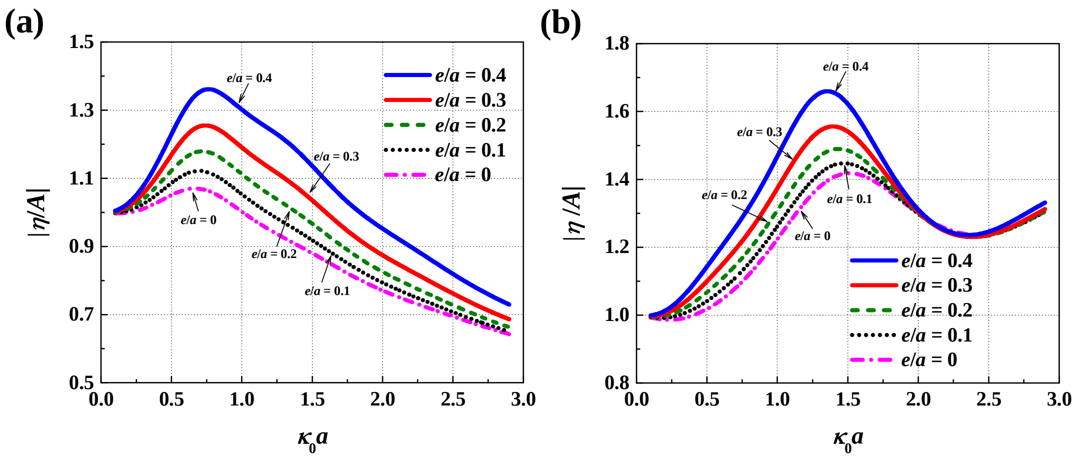

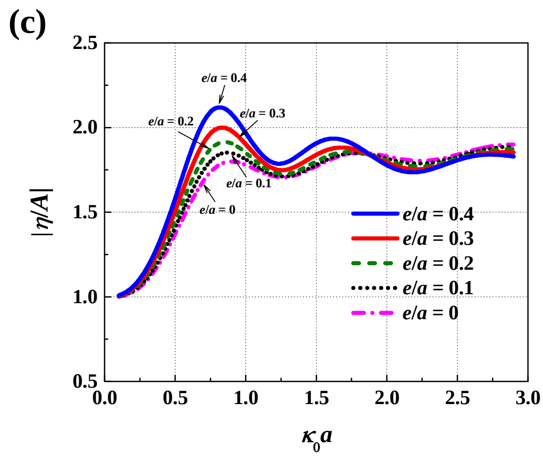

Fig. 9 Normalized linear wave runup amplitude at three locations around the body with different plate height (T/a = 1, R/a = 1.5, d/a = 3) (a) $r = a$, $\theta = 0$ (b) $r = a$, $\theta = \pi/2$ (c) $r = a$, $\theta = \pi$

The distribution of the wave elevation amplitude around the body is plotted in Figs. 10-12 for $\kappa_0 a$ = 0.67, 0.74 and 1.5 respectively with the plate height fixed at e/a = 0.1 and the plate radius varies as R/a = 1, 1.5 and 2. All wave patterns are characterized by obviously amplified free-surface oscillation near the front edge. At $\kappa_0 a$ = 0.67 and 0.74 (see Figs. 11-12), the wave elevation around the front and the rear edges shows an increasing tendency as R increases. In addition, at $\kappa_0 a$ = 0.67 and 0.74, the increase of R leads to obvious changes in the wave pattern in the downstream region. Meanwhile, the wave elevation and its distribution at $\kappa_0 a$ = 1.5 (see Fig. 13) appears to be less dependent on the plate radius. This may be due to the fact that the wave motion attenuates more rapidly in the gravity direction as the wave length decreases. Short waves may not experience strong interaction with a plate submerged at a certain depth and then obvious disturb on the wave field cannot be induced.

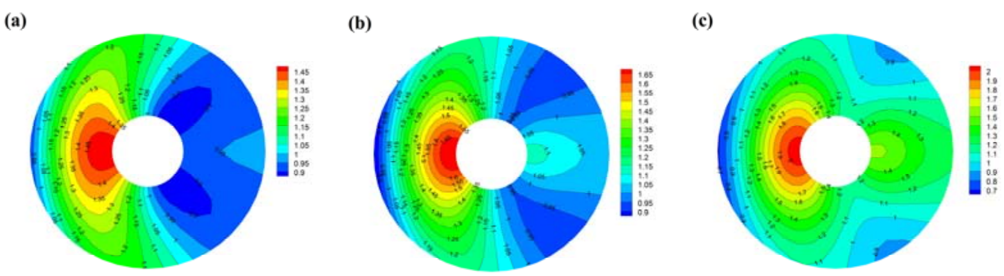

Fig. 10 Distribution of the normalized wave elevation amplitude around the body at $\kappa_0 a$ = 0.67 (T/a = 1, e/a = 0.1, d/a = 3) (a) R/a = 1 (b) R/a = 1.5 (c) R/a = 2

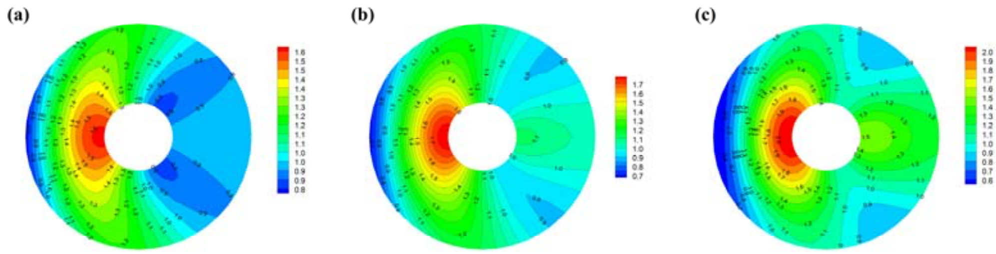

Fig. 11 Distribution of the normalized wave elevation amplitude around the body at $\kappa_0 a$ = 0.74 (T/a = 1, e/a = 0.1, d/a = 3) (a) R/a = 1 (b) R/a = 1.5 (c) R/a = 2

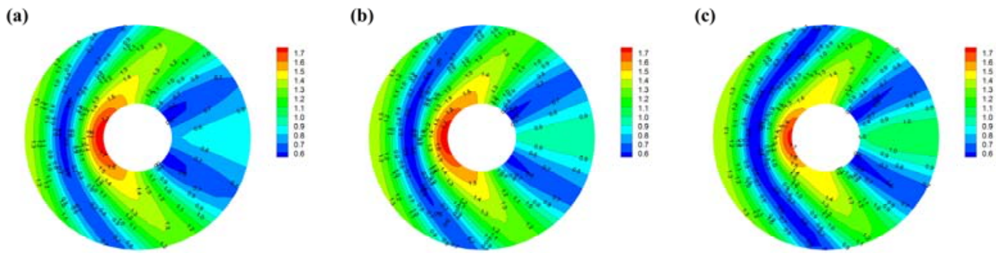

Fig. 12 Distribution of the normalized wave elevation amplitude around the body at $\kappa_0 a$ = 1.5 (T/a = 1, e/a = 0.1, d/a = 3) (a) R/a = 1 (b) R/a = 1.5 (c) R/a = 2

7.2 Linear Wave Force

The variation of the linear wave force amplitude is shown in Fig. 13 for different plate radius R with the plate height being constant as e/a = 0.1. Note from Fig. 13(a) that regardless of the plate height the horizontal force firstly increases quickly until it reaches the maximum, and then decreases continuously as $\kappa_0 a$ increases further. The hydrodynamic pressure along the waterline is directly proportional to the wave elevation. When $R = a$, the peak value occurs around $\kappa_0 a$ = 0.87, at which the relative phase between the wave elevation around the front and the rear edges is 158 degrees. It corresponds to the situation that that when a wave crest appears around the front edge, leading to positive hydrodynamic pressure, negative pressure occurs simultaneously around the rear edge. In addition, when the peak value occurs at $R = a$, an increase in R can amplify the free-surface oscillation around the front and rear edges and increase their relative phase gradually at the mean time, which can give rise to the increase of the horizontal wave force. Therefore, the peak values in Fig. 13(a) increase as R increases. Note from Fig. 13(b) that the vertical force decreases continuously as $\kappa_0 a$

increases when there is no plate attached to the column ($R = a$). Things become different when $R > a$, as there exist a zero-excitation frequency at which the structure endures no vertical excitation force. Basically, the vertical force can be divided into two parts, one the force on the bottom of the plate and the other the opposite one on the upper surface of the plate. The summation of the two parts can reach zero when they have the same magnitude. The zero-excitation frequency, moves gradually to the low frequency region as R increases. Before the zero-excitation point, an attached plate with larger radius endures smaller vertical force, while beyond that point such tendency is reversed but more pronounced.

Fig. 14 presents the linear wave force amplitude for different plate height e with the plate radius being constant as R/a = 1.5. In Fig. 14, the variation trend of the results with $\kappa_0 a$ is typical similar to that in Fig. 13. The horizontal force in general increases as e increases at a fixed wave frequency. Again, the vertical force is found to be zero at specific frequencies which gradually moves to the low frequency region as the plate height increases.

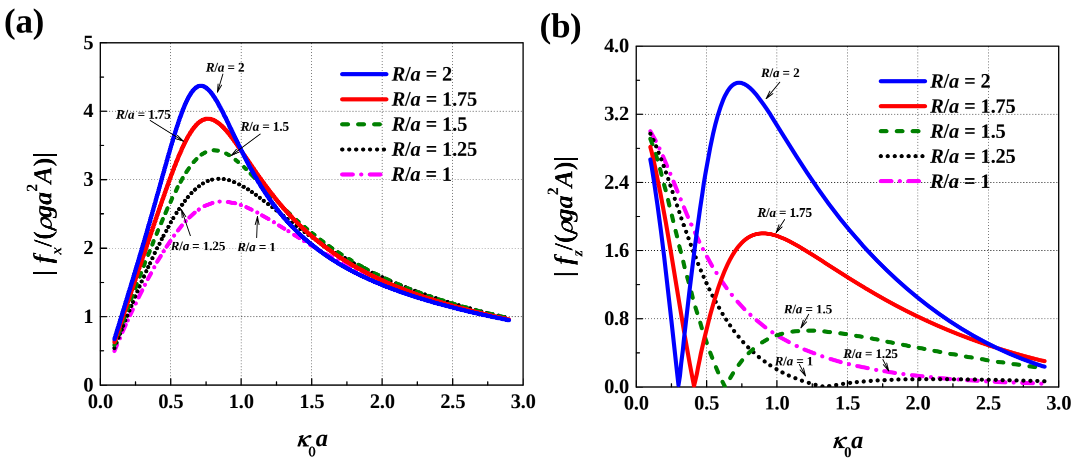

Fig. 13 Normalized linear wave force amplitude with different plate radius (T/a = 1, e/a = 0.1, d/a = 3) (a) horizontal force (b) vertical force

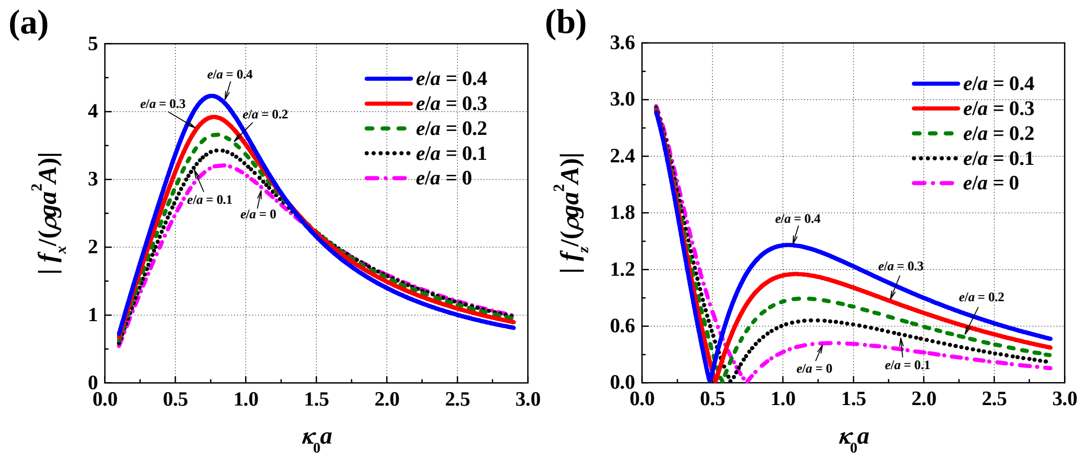

Fig. 14 Normalized linear wave force amplitude with different plate height ($T/a = 1$, $R/a = 1.5$, $d/a = 3$) (a) horizontal force (b) vertical force

7.3 Mean Drift Force

The influence of the plate radius on the mean drift force is examined in Fig. 15 with the plate height fixed at $e/a = 0.1$. The results given in this section are all obtained based on the derived mean drift force formulation. In Fig. 15(a), the mean drift force in the horizontal direction in general increases as R increases at a fixed wave frequency. As shown in Eq. (33), the mean drift force in the horizontal direction can be split into two terms: one written on the control surface and the other the wave elevation term. The two terms decrease to zero in the zero-frequency limit and then follow opposite variation trend with $\kappa_0 a$. In the high frequency region, their joint contribution is nearly constant, leading to the overall force tends to behave stable. From Fig. 15(b), it is noted that mean drift force in the vertical direction is in the negative z-direction over the entire frequency domain when $R = a$. This does not hold true when $R > a$. Apparently, the vertical mean drift force is contributed by two opposite parts which are associated with the wave action over the upper and bottom surfaces of the plate respectively. The overall force is firstly dominated by the later part which remains negative over all frequencies and its magnitude gradually decreases to zero as $\kappa_0 a$ increases. As $\kappa_0 a$ increases further, the former part becomes predominant, leading to the overall force in the positive z-direction. From Fig. 15(b), it is also noted that a larger plate radius results in more prominent variation against $\kappa_0 a$.

The variation of the mean drift force against the plate height e is shown in Fig. 16

when the plate radius keeps constant as R/a = 1.5. Effects of the plate height are similar to that of the plate radius. Generally, shallower heave plates (larger e) can more effectively interact with surface waves to affect the wave scattering process. Therefore, a plate with a larger height can impose more significant effects on the force.

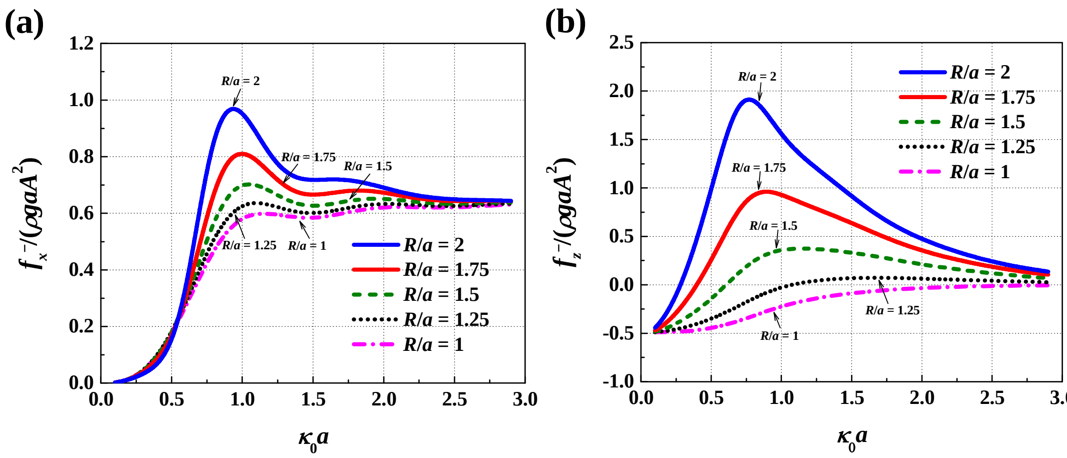

Fig. 15 Normalized mean drift force with different plate radius (T/a = 1, e/a = 0.1, d/a = 3) (a) horizontal force (b) vertical force

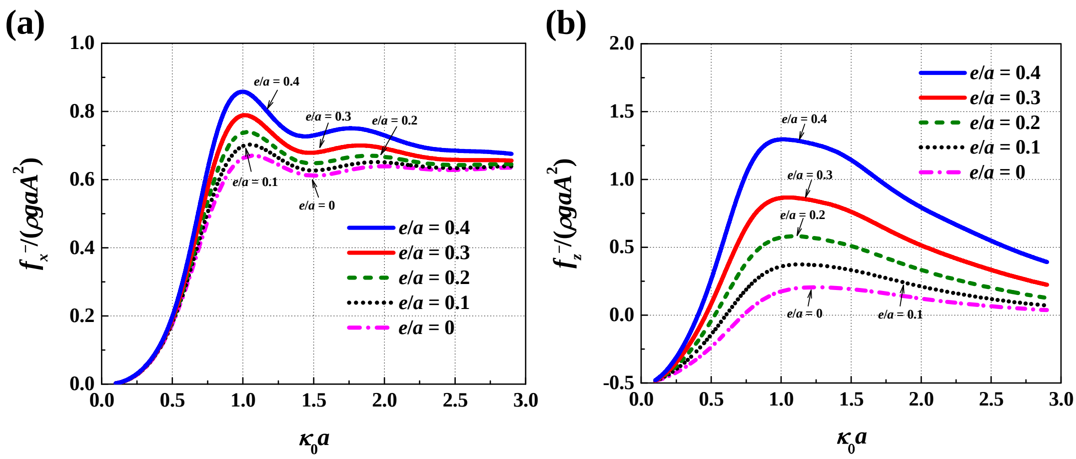

Fig. 16 Normalized mean drift force with different plate height (T/a = 1, R/a = 1.5, d/a = 3) (a) horizontal force (b) vertical force

8. Conclusions

Wave interaction with a floating column with a submerged plate attached at the bottom is investigated through applying a theoretical model. Emphasis of this study has been laid on the influence of the attached plate on the wave force and the associated wave runup. Extensive calculations have been conducted with a variety of geometrical parameters. The main conclusions can then be summarized as follows:

1) A novel derivation of the mean drift force formulation is developed based on the

application of the Green's second identity to the velocity potential and its derivative in finite fluid volume surrounding the body. The derived formulation involves control surfaces at a distance from the body and is found to be essentially identical with that in Chen (2006), which is developed by using the variants of Stokes's and Gauss's theorem, for cases of stationary and wall-sided bodies. Semi-analytical solutions of the mean drift force on the compound column-plate structure are developed based on respectively the derived and the classic far-field formulations. Those solutions both possess good convergence and the results based on them agree well with each other.

2) The existence of the plate can notably disturb the wave scattering process related to a column. At specific frequencies, obvious amplification of the free-surface oscillation can be observed around the front and the rear edges of the column after including the effects of the plate. Correspondingly, local pressure on the body can be obviously increased, which is not beneficial to the structural safety.

3) In the horizontal direction, the linear wave force and mean drift force both increase as the plate radius or height increases. In the vertical direction, the linear wave force and mean drift force on a column with an attached plate follow a substantially different behavior from that without the plate and can vanish at specific frequencies due to the cancellation between the wave action on the bottom and the upper surfaces of the plate, which suggests that the attached plate can be optimized to decrease the vertical force through adjusting the design parameters.

Acknowledgement

The work is financial supported by the National Natural Science Foundation of China (Grant Nos. 51479026 and 51679036).

Reference

1. Antonutti R, Peyrard C, Johanning L, et al. An investigation of the effects of wind-induced inclination on floating wind turbine dynamics: heave plate excursion. Ocean Engineering, 2014, 91(15): 208-217.
2. Bachynski E E, Kvittem M I, Luan C, et al. Wind-wave misalignment effects on floating wind turbines: motions and tower load effects. Journal of Offshore Mechanics & Arctic Engineering, 2014, 136(4): 041902.

3. Calisal S M, Sabuncu T. Hydrodynamic coefficients for vertical composite cylinders. Ocean Engineering, 1984, 11(5): 525-542.
4. Chen X B. Middle-field formulation for the computation of wave-drift loads. Journal of Engineering Mathematics, 2006, 59(1): 61-82.
5. Downie M J, Graham J M R, Hall C, et al. An experimental investigation of motion control devices for truss spars. Marine Structures, 2000, 13(2): 75-90.
6. Farina L. Water wave radiation by a heaving submerged horizontal disk very near the free surface. Physics of Fluids, 2010, 22(5): 057102.
7. Jiang S C, Gou Y and Teng B. Water Wave Radiation Problem by a Submerged Cylinder. Journal of Engineering Mechanics, 2014, 140(5): 06014003.
8. Jiang S C, Gou Y, Teng B, et al. Analytical solution of a wave diffraction problem on a submerged cylinder. Journal of Engineering Mechanics, 2014, 140(1): 225-232.
9. Koh H J and Cho I H. Heave motion response of a circular cylinder with the dual damping plates. Ocean Engineering, 2016, 125: 95-102.
10. Lee C H. On the evaluation of quadratic forces on stationary bodies. Journal of Engineering Mathematics, 2007, 58(1-4): 141-148.
11. Li B -B, Huang Z -H, Low Y M, et al. Experimental and numerical study of the effects of heave plate on the motion of a new deep draft multi-spar platform. Journal of Marine Science and Technology, 2013, 18(2): 229-246.
12. Martin P A and Farina L. Radiation of water waves by a heaving submerged horizontal disc. Journal of Fluid Mechanics, 1997, 337: 365-379.
13. Maruo H. The drift of a body floating in waves. Journal of Ship Research, 1960, 4: 1-10.
14. Mei C C, Stiassnie M, Yue D K -P. Theory and applications of ocean surface waves. 2005, World Scientific, Singapore.
15. Molin B. On the added mass and damping of periodic arrays of fully or partially porous disks. Journal of Fluids and Structures, 2001, 15(2): 275-290.
16. Newman J N. The drift force and moment on ships in waves. Journal of Ship Research, 1967, 11: 51-60.
17. Ogilvie T F. Second order hydrodynamic effects on ocean platforms. In: Proceedings of International Workshop on Ship and Platform Motions, University of California, Berkeley, USA, Oct 26-28 1983, pp. 205-265.
18. Pinkster J A. Low frequency second order wave exciting forces on floating structures. PhD Thesis, Delft University of Technology, the Netherlands, 1980.
19. Tao L -B, Thiagarajan K. Low KC flow regimes of oscillating sharp edges I. Vortex shedding observation. Applied Ocean Research, 2003, 25(1): 21-35.
20. Tao L -B, Thiagarajan K. Low flow regimes of oscillating sharp edges. II. Hydrodynamic forces. Applied Ocean Research, 2003, 25(2): 53-62.
21. Wang K, Zhang Z -Q. Study on hydrodynamic coefficients of double submerged inclined plates. China Ocean Engineering, 2018, 32(1): 85-89.

22. Yeung R W. Added mass and damping of a vertical cylinder in finite-depth waters. Applied Ocean Research, 1981, 3(3): 119-133.
23. Yu X -P. Functional performance of a submerged and essentially horizontal plate, for offshore wave control: a review. Coastal Engineering Journal, 2002, 44(02): 127-147.
24. Yu X -P and Chwang A T. Analysis of wave scattering by submerged circular disk. Journal of Engineering Mechanics, 1993, 119(9): 1804-1817.